Highlights

1. A porous carbon fibers micro-scaffold with Sn-modified surface is fabricated via electrospinning and hard template method.

2. Porous carbon fibers lower the local current and electric field density, leading to homogeneous Zn^{2+} flux.

3. Zincophilic Sn has a high adsorption energy towards Zn^{2+} and reduces the HER tendency.

4. Outstanding rate performance and cycling stability are realized in NaVO||Sn-PCF@Zn full cells.

Table of Content Entry

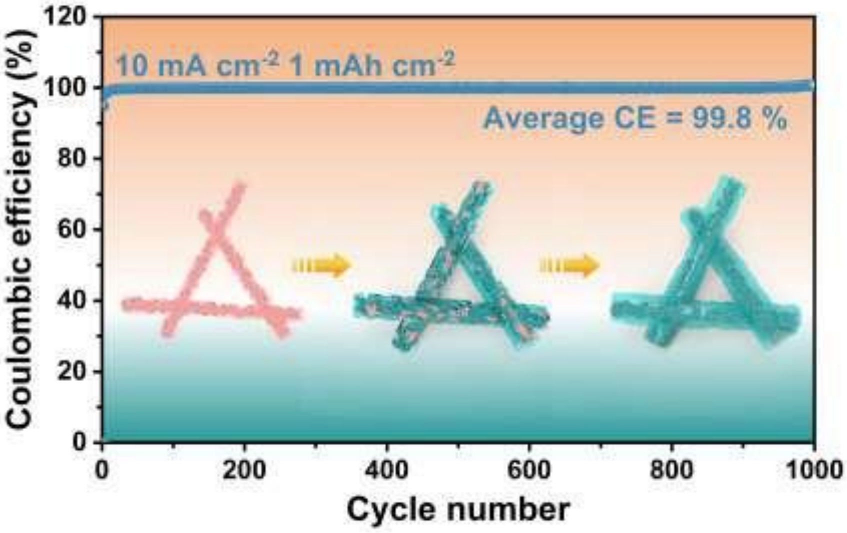

3D zincophilic micro-scaffold enables stable Zn deposition

Jin-Lin Yang[a,1], Peihua Yang[b,1], Wenqi Yan[a], Jian-Wei Zhao[c], and Hong Jin Fan[a,]*

[a] School of Physical and Mathematical Sciences, Nanyang Technological University, Singapore 637371, Singapore

[b] The Institute of Technological Sciences, Wuhan University, Wuhan 430072, China

[c] Shenzhen HUASUAN Technology Co. Ltd, Shenzhen 518055, China

[1] These authors contributed equally to this work.

* Corresponding author. Email: fanhj@ntu.edu.sg (H.J. Fan)

Keywords: Zn metal anode, zincophilic micro-scaffold, Zn electrodeposition, Zn dendrites, Zn-ion battery

ABSTRACT: Aqueous zinc ion battery is promising technology for safe and low-cost energy storage. However, zinc batteries using metallic Zn anode suffer from poor cycle life due to Zn dendrites growth, side reactions and parasitic byproducts. To tackle these issues, we design a potent Zn anode host by combining two strategies: 3D microporous scaffold with zincophilic surfaces, which proves advantageous in stabilizing Zn metal deposition and improving the cycle life of full cells. Specifically, a Sn nanodots coated porous carbon fiber (Sn-PCF) network has been carefully designed. The PCF network is conducive in promoting homogeneous Zn^{2+} flux and uniform 3D Zn nucleation, leading to dense and flat Zn deposition even under a high capacity of 10 mAh cm^{-2}. Meanwhile, experiments and calculation reveal that, the Sn nanodots coating induces a strongly zincophilic surface of each fiber with high Zn^{2+} adsorption and surface immobilization. This guarantees a high reversibility of Zn plating/stripping compared to PCF without Sn coating or other non-3D hosts. The advantage of this 3D Sn-PCF host is demonstrated in both symmetric cells and full device paired with $Na_2V_6O_{16}$ cathode.

Keywords: Zn metal anode, zincophilic micro-scaffold, Zn electrodeposition, Zn dendrites, Zn-ion battery

1. Introduction

The increased demand for the electric vehicles and portable devices with high safety, long cycling life and low cost cannot be fulfilled by the current lithium-ion batteries. Among various options, rechargeable aqueous Zn batteries (AZBs) are widely regarded as potential candidates for next-generation energy storage system owing to the suitable Zn redox potential (−0.764 V vs SHE), high theoretical gravimetric capacity (820 mAh g^{-1}) and volumetric capacity (5855 mAh cm^{-3}), and eco-friendliness [1-4]. Although significant achievements have been obtained in the past several years for AZBs, the pitfalls persist. They include uncontrolled Zn dendrites formation, surface corrosion and hydrogen evolution reaction, which result in low Coulombic efficiency (CE) and energy efficiency [5-8]. The growth of Zn dendrites greatly increases the surface roughness and will aggravate the 'dead Zn' formation or puncture the separator. Additionally, the inhomogeneous dendrites distribution may also boost the side reaction and surface corrosion because of the high local current density [9, 10]. Therefore, Zn dendrites suppression is considered as a critical while challenging task for AZBs.

Zn dendrite formation is determined by nucleation and growth behavior. Inhomogeneous nucleation will result in 2D hexagonal platelet-like Zn dendrites. Thus, the Zn deposition is strongly influenced by the zincophilicity, local current/electric field density, and the nucleation sites distribution on the electrode [11, 12]. Enormous efforts have been made to realize dendrite-free Zn-metal anode such as using concentrated electrolyte, constructing protective layer and optimizing electrolyte composition [13-18]. Despite the progress in common planar configuration, host-less Zn anode still undergoes huge volume fluctuation during long-term plating/striping process. Besides, external factors include the electrode surface morphology and ion-diffusion are also rarely involved.

Fabricating 3D Zn host with high surface area is considered as an effective method to uniformize the local current density and Zn ions flux. Some skeletons such as 3D sponge Zn [19], Cu foams [20], 3D Ni lattice [21], carbon clothes [22], MOFs [23] and CNTs [24, 25] are previously reported. However, the volume utilization of the host, Zn nucleation morphology, rational channels/pores size design, hydrogen evolution reaction (HER) prohibition, and the integration of conductivity and zincophilicity have not been systematically investigated yet. More importantly, to elevate the 2D surface diffusion barrier of Zn ions during the plating process and simultaneously guide dense Zn accumulation on the host is still a challenge. Recently, porous carbon fibers (PCF)-based framework synthesized via electrospinning technology combined with hard-templating method has been widely adopted in lithium-metal/sulfur batteries [26, 27]. Owing to the hollow structure of fibers and abundant interspaces within the fibers network, robust electrode with higher energy density can be realized.

To fulfil the multiple requirements mentioned above, in this work, we design a unique 3D PCF-based micro-scaffold with Sn modification (Sn-PCF). The rational is as follows. The 3D crosslinked conductive carbon fiber network coupled with highly zincophilic Sn nanodots efficiently eliminates the ‘tip effect’ by uniformizing the current density and Zn^{2+} flux, and also constructs a physical confinement for dendrites. Metallic Sn exhibits a strong Zn^{2+} adsorption and high Zn^{2+} surface diffusion barrier, which is the key to the regulated nucleation and homogeneous Zn deposition on individual fibers. Simultaneously, the Sn coating also lowers the HER tendency. These merits synergistically promote lead to highly reversible Zn plating/stripping. Zn-ion battery full cells by pairing $Na_2V_6O_{16}\cdot 1.63H_2O$ (NaVO) cathode and Sn-PCF@Zn anode show an ultralow capacity decay rate around 0.009 % and 0.010 % per cycle at the current densities of 5 A g^{-1} and 10 A g^{-1} (during 2000 cycles), respectively. The presented strategy provides a new avenue for stable Zn anode design based on the 3D host with highly integration of conductivity and zincophilicity.

2. Results and discussion

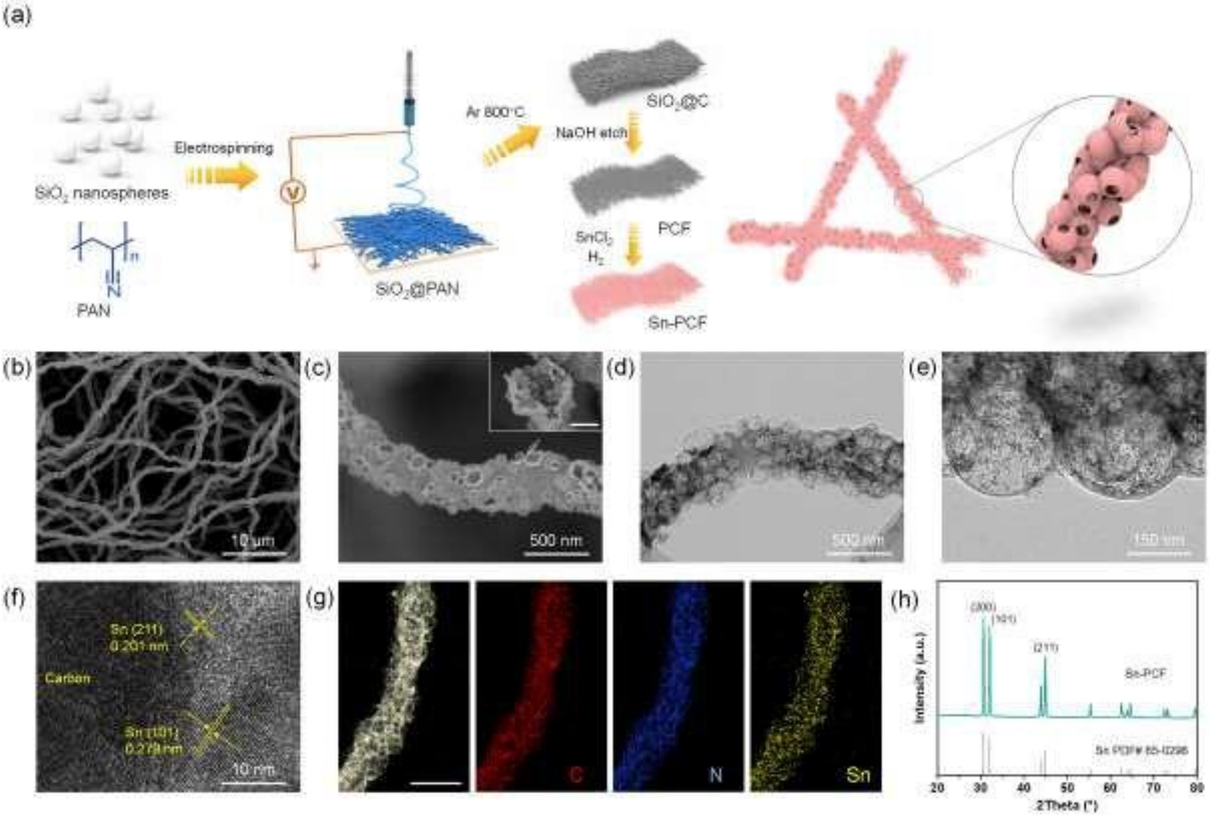

Fig. 1 Fabrication and morphology of Sn-PCF. (a) Schematic of the fabrication process. (b-c) SEM images. Inset scale bar: 200 nm. (d-e) TEM images. (f) HRTEM image. (g) Element mappings. (h) XRD patterns.

Fig. 1a and Fig. S1 schematically show the multistep hard-template fabrication process of Sn-PCF (more details of the synthesis process are presented in Supporting Information). Monodispersed SiO_2 nanospheres with an average diameter around 150 nm were synthesized via a classic Stöber method and used as the templates to create the pores (Fig. S2). The as-prepared SiO_2 nanospheres were mixed with PAN in DMF and the mixture were electrospun to form the SiO_2@PAN nanofibers. After carbonization in Ar at 800 °C, all the SiO_2 nanospheres are well wrapped by a carbon layer in each fiber without any cracks (Fig. S3). After the SiO_2 template was etched by NaOH, amorphous PCF with interconnected hollow pores were obtained (Fig. S4 and S5). The PCF fibers was then modified by nanosized

Sn using an existing solution coating method [28, 29] followed by thermal reduction. After the Sn modification, the resultant Sn-PCF also exhibits hierarchical hollow structures with spherical voids packed in a space-efficient arrangement (Fig. 1b-d, Fig. S6). The nanosized Sn dots can be observed on the carbon shell of PCF (Fig. 1e), where the lattice fringes with interplanar spacings of 0.201 and 0.279 nm can be assigned to the (211) and (101) planes of Sn, respectively (Fig. 1f) [22, 30, 31]. C, Sn, N are all homogeneously distributed on the fiber (Fig. 1g), indicating a uniform Sn coating. XRD pattern of Sn-PCF further confirms the complete conversion from SnO_2 to Sn with a clear identification of metallic Sn (Fig. 1h).

The composition and morphology of Sn-PCF sample was further characterized. X-ray photoelectron spectroscopy (XPS) in Fig. S7 show that the PCF sample exhibits co-existence of C−C, C=C and C=O. The C−N bonds and four different states of N atoms detected in N 1s spectrum can be attributed to the inheritance of N from PAN during the calcination process [26]. Consistent with the XRD result, Sn 3d spectrum certifies the existence of metallic Sn^0 [32]. In the TG-DSC measurement, the sudden drop of the weight around 400 ^oC is caused by the oxidation of carbon (Fig. S8) [28]. At the same time, Sn is also oxidized and increases steadily the mass before 700 °C [33]. The remaining SnO_2 content is ~ 65 wt%, considering that the Sn weight percentage in SnO_2 is 78.8 wt%, thus the average mass content of Sn in Sn-PCF can be calculated around 51 wt%. The Raman spectra suggest that only the typical G peak and D peak of graphite can be detected in the Sn-PCF and PCF (Fig. S9a), demonstrating a stable graphitic degree during the Sn modification process. To characterize the pore structure of Sn-PCF, Brunauer–Emmett–Teller (BET) analysis and N_2 adsorption/desorption isotherms were employed. Together with the average pore size around 30 nm, Sn-PCF delivers a specific surface area around 117 m^2 g^{-1} (Fig. S9b), higher than that of the PCF owing to the nanoparticles modification. It is expected that such a porous hierarchical structure will benefit sufficient contact between the 3D host and Zn^{2+} as well as the fast ions transfer throughout the whole scaffold [34].

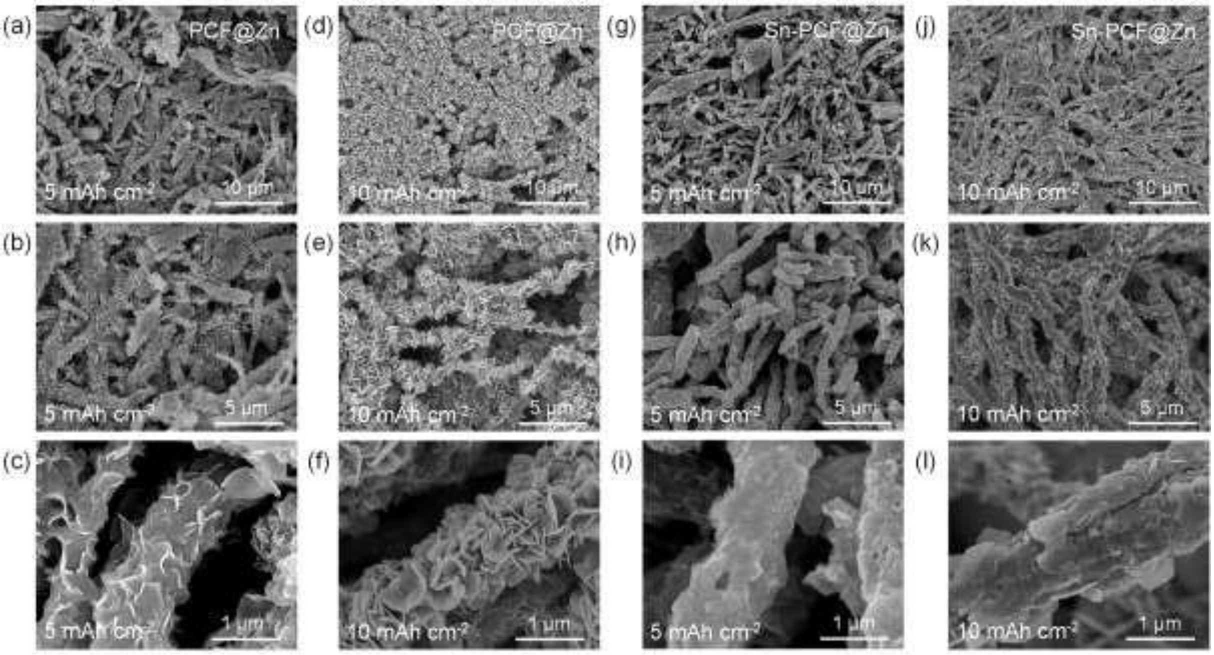

Fig. 2 Morphology of Zn deposition on different hosts. SEM images of PCF after Zn plating at various capacities: (a-c) 5 mAh cm^{-2}, d–f) 10 mAh cm^{-2}. SEM images of Sn-PCF after Zn plating with various capacity: (g-i) 5 mAh cm^{-2}, (j-l) 10 mAh cm^{-2}. The current density for Zn deposition was 1 mA cm^{-2}.

To exam the Zn deposition morphology on the new electrode, bare Cu foil, PCF, and Sn-PCF were probed at a current density of 1 mA cm^{-2} with a Zn foil as the counter electrode. When Zn is plated with a capacity of 5 mAh cm^{-2}, PCF exhibits fewer sheets-like Zn dendrites than that on Cu foil (Fig. 2a-c, S10), which can be explained by the uniformized electric field on such porous architecture. In sharp contrast to PCF, Sn-PCF demonstrates a smooth Zn precipitation and almost no planar Zn dendrites can be found (Fig. 2g-i). When increasing the deposition capacity to 10 mAh cm^{-2}, the Zn dendrites on Cu foil become larger, up to a size over 2 μm for some deposited plates. A crowded flake structure of deposited Zn can be observed on PCF, indicating that the Zn nucleation is still inhomogeneous and irregular (Fig. 2d-f). Coming to the Sn-PCF, a flat and dense surface is observed with only a few flake-like Zn dendrites (Fig. 2j-l), suggesting that the Sn modification can efficiently generate a homogeneous Zn nucleation.

It is important that the inner space is fully accessed during the Zn plating process. As shown in Fig. S11, with a deposition capacity of 10 mAh cm^{-2}, bare Cu foil with planar surface exhibits uncontrolled Zn protrusions growth with a loose accumulation, while all the carbon fibers in PCF are covered by rampant Zn nanosheets with partial Zn dendrites on the outer surface of electrode. In contrast, the Sn-PCF electrode not only shows a complete coverage of Zn on individual fibers but also keeps a dendrite-free outer surface, demonstrating a higher spatial utilization and a uniform Zn deposition than that on PCF. Top-view digital photographs of PCF@Zn and Sn-PCF@Zn further verify that the latter could accommodate large amount of Zn with high density and prevent the protuberant dendrites (Fig. S12). To figure out whether all the deposited Zn can reversibly participate in the subsequent stripping process, both PCF and Sn-PCF after the 10 mAh cm^{-2} Zn deposition test were charged subsequently with a cutoff potential of 0.5 V vs Zn/Zn^{2+}. As shown in Fig. S13, although Zn is fully stripped from PCF, sheets-like byproducts or dendrites can still be found in the PCF framework. In sharp contrast, the Sn-PCF almost retains its initial morphology before the deposition test, indicating a higher redox reversibility.

To deeply understand the mechanism of dendrite suppression on Sn-PCF, the interaction between Zn ion and different substrates were analyzed from a theoretical aspect. First, DFT method was adopted to investigate the adsorption energies of carbon and different Sn planes to Zn ions. The bonding energies of Zn^{2+} on carbon, Sn (211), Sn (200) and Sn (101) are −0.21, −0.96, −0.58, and −1.14 eV, respectively, substantiating that Sn can possess stronger Zn^{2+} adsorption than carbon (Fig. 3a). In addition, although a certain amount of N from PAN remains on PCF, it makes little contribution to Zn deposition because nitrogen presents a similar Zn^{2+} binding energy compared to carbon according to the previous studies [35, 36]. Based on the interfacial charge-density diagrams of different adsorption models (inset of Fig.

3a), the charge densities of the Sn atoms on the bulk surface become lower and electrons tend to accumulate at the middle sites between Zn ion and Sn. The reduced charge density can be further confirmed by the XPS spectra of Sn $3d_{5/2}$, which depicts a positive peak shift after Zn deposition (Fig. 3b) [32, 37]. According to the optimized configurations and the corresponding barriers of the Zn^{2+} diffusion pathways on different substrates (Fig. 3c and 3e), Sn demonstrates much higher surface diffusion barriers than that of carbon. That implies that the Sn coating makes it hard for adsorbed Zn ions to diffuse laterally. Hence, as elucidated in Fig. 3d, a 3D Zn accumulation can be realized on Sn-PCF with an even and dense morphology. However, for the PCF without Sn modification, it corresponds to a lower zincophilicity and stronger tendency of Zn^{2+} diffusion on the surface, resulting in localized growth into the sheets-like dendrites.

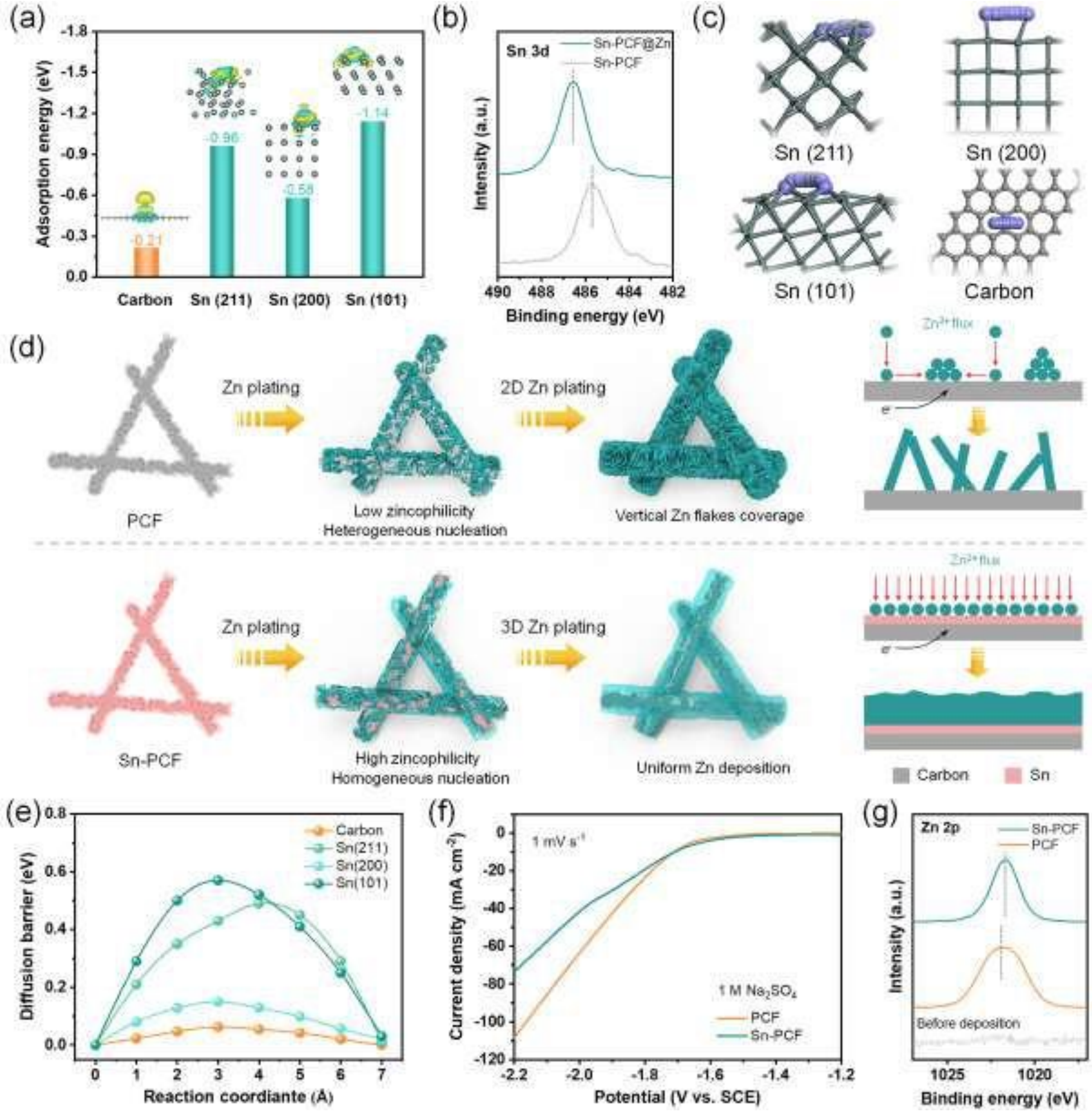

Fig. 3 Mechanism of the Zn nucleation. a) DFT calculation results of the adsorption energy of Zn ion on different substrates with the diagrams of charge density. b) XPS spectra of Sn $3d_{5/2}$ before and after Zn plating. c) Optimized structures of the Zn ion diffusion pathways on different substrates and the corresponding f) diffusion barriers. d) Zn plating and nucleation diagrams on PCF and Sn-PCF. f) LSV curves of Sn-PCF and PCF in 1 M Na_2SO_4 at 1 mV s^{-1}. g) XPS spectra of Zn $2p_{3/2}$ after Zn deposition.

In addition to the dendrite suppression, HER prohibition on Zn host is also crucial to guarantee the high CE with fast redox kinetics. As shown in the linear sweep voltammetry (LSV) curves (Fig. 3f), Sn-PCF electrode demonstrates a higher HER overpotential than PCF. Correspondingly, Zn $2p_{3/2}$ peak of Sn-PCF after Zn deposition exhibits a lower binding energy than that of the PCF after deposition (Fig. 3g), indicating that more Zn^{2+} form on PCF because of the formation of the HER byproducts ($Zn_4SO_4(OH)_6\cdot5H_2O$, ZSH) [38]. In addition, the XRD reflections of ZSH are more intense in PCF than that of Sn-PCF after Zn deposition (Fig. S14). This lower HER tendency will also contribute to homogeneous Zn deposition on Sn-PCF, which is conducive to the Zn anode lifespan.

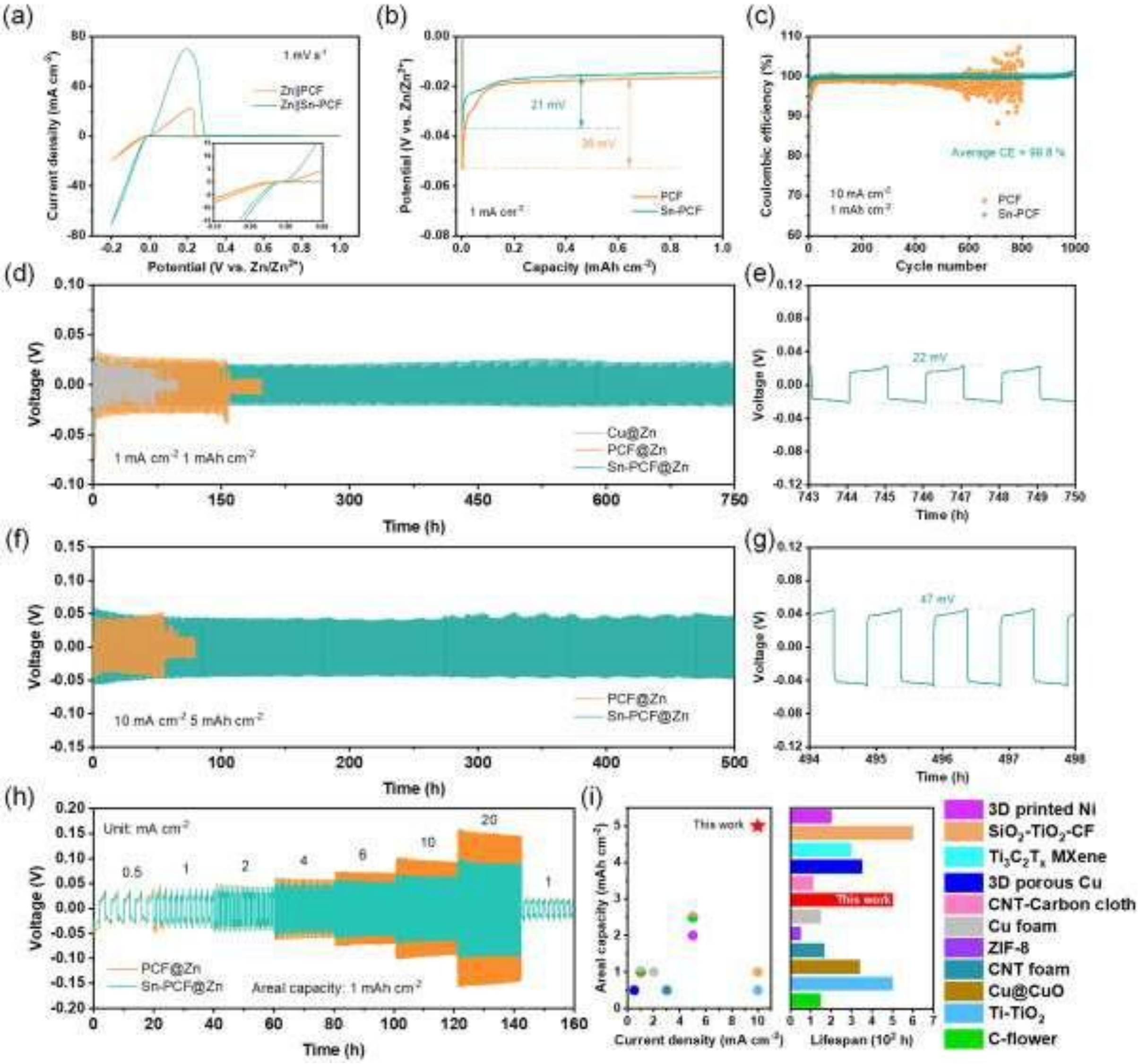

Fig. 4 Zn plating/stripping kinetics, reversibility, and stability in symmetric cells. Two types of current collectors, PCF and Sn-PCF are tested in comparison in a 2 M $ZnSO_4$ electrolyte. a) CV curves. b) Zn plating profiles at 1 mA cm^{-2}/1 mAh cm^{-2}. c) Coulombic efficiencies at 10 mA cm^{-2}/1 mAh cm^{-2}. d-g) Voltage-time curves at conditions of 1 mA cm^{-2}/1 mAh cm^{-2} and 10 mA cm^{-2}/5 mAh cm^{-2}. h) Rate capability of symmetric cells from 1 to 20 mA cm^{-2}. i) Comparison of the current density, areal capacity and lifespan of symmetric cells with

Sn-PCF@Zn and previously reported Zn hosts.

Electrochemical examination of the Zn plating/stripping dynamics and reversibility is conducted in half cells using Zn as the counter electrode. First, in the cyclic voltammetry (CV) test, the Sn-PCF electrode exhibits a higher response current and smaller potential separation compared to PCF (**Fig. 4**a), implying that the Zn nucleation can be effectively induced on Sn-PCF with a fast reaction kinetics. Such improved redox dynamics can be also revealed from the nucleation overpotential. As shown in Fig. 4b and S15a, the nucleation overpotential on Sn-PCF is 21 mV, much lower than that on PCF (36 mV) and Cu foil (86 mV) at 1 mA cm^{-2}. When increasing the current density to 5 mA cm^{-2} and 10 mA cm^{-2}, the nucleation overpotential on Sn-PCF are 25 and 46 mV, respectively, still lower than that of PCF (Fig. S15b-c), further confirming the abundant accessible active sites for Zn deposition.

Next aspect is the coulombic efficiency (CE). We obtained a stable Zn plating/stripping behavior on Sn-PCF with average CE values around 95.0 % and 98.2 % at the current densities of 1 and 5 mA cm^{-2}, respectively (Fig. S16a-b). Meanwhile, the half cells based on Cu foil or PCF fail quickly with drastically lower and unstable CE values. Regarding the plateau overpotential, Sn-PCF demonstrates the lowest voltage separation of around 17.5 and 48.7 mV at 1 and 5 mA cm^{-2}, respectively (Fig. S16c-d). With a higher current density of 10 mA cm^{-2}, the average CE of Sn-PCF still maintains over 99.8 % at the areal capacities of 1 mAh cm^{-2} over 1000 cycles (Fig. 4c). Even the deposition capacity is increased to 5 mAh cm^{-2}, the CE keeps around 98.3 % after 250 cycles (Fig. S16e). The presented redox kinetics and reversibility confirm that the Zn can be stabilized on Sn-PCF, which is believed to be a result of numerous accessible nucleation sites, reduced local current density and alleviation of side reactions.

The effectiveness of Sn-PCF on Zn anode cycling stability was illustrated by the symmetric cells test. The potential profiles for Zn striping/plating at different current densities and certain capacities are monitored. As shown in Fig. 4d and 4e, with a capacity of 1 mAh cm^{-2}, the cell with Sn-PCF@Zn electrodes shows stable potential profile with a polarization around 22 mV over 750 h at 1 mA cm^{-2}. In contrast, bare Cu foil and PCF are short after 75 and 150 h, respectively. Such stability can also be achieved at 5 mA cm^{-2} where the Sn-PCF@Zn performs a polarization around 37 mV with a superior lifespan over 700 h (Fig. S17). A sudden rise of the voltage in PCF@Zn at 5 mA cm^{-2} can be attributed to the passivation caused by side-reaction products.[37] Notably, when the current density goes up to 10 mA cm^{-2} with a areal capacity of 5 mAh cm^{-2} (50 % of the total areal capacity on as-prepared Zn-contained electrode, Fig. 4f and 4g), Sn-PCF@Zn still demonstrates an elongated cycling life over 500 h with a voltage hysteresis of 47 mV, much longer than that of the PCF@Zn (~60 h). In terms of rate performance, as shown in Fig. 4h, lower hysteresis can be observed on Sn-PCF@Zn. These results underpin the excellent stability of Zn anode endowed by Sn-PCF. A comparison of long-term cycling performance of our Sn-PCF@Zn with other reported Zn hosts is shown in Fig. 4i [21, 25, 34, 35, 39-42].

We further assembled Zn||NaVO full cells to explore the feasibility of fabricated Sn-PCF@Zn anode for practical applications. The synthesized NaVO nanowires possess a crystalline structure in good agreement with the standard card ($P2_1/m$, JCPDS: 16-0601), and exhibit a well integration with graphene (Fig. S18). Sodium ions serve pillars in the interlayer of V_3O_8 framework, which enables a stable H^+/Zn^{2+} co-insertion/extraction process [43, 44]. CV curves at a scan rate of 0.5 mV s^{-1} show that the full cell with Sn-PCF@Zn anode has a narrower peak separation and higher peak currents (**Fig. 5**a) that that assembled with PCF@Zn anode, indicating an accelerated redox kinetics in the former [45]. In the rate capability test (Fig. 5b and 5c), Sn-PCF@Zn||NaVO battery displays the initial discharge capacities of 361, 298, 267, 219, 187, and 142 mAh g^{-1} at 0.2, 0.5, 1, 3, 5, and 10 A g^{-1}, respectively. The inferior rate performance in PCF@Zn||NaVO can be assigned to the charge transfer limitation caused by the lower special utilization and rampant planar Zn dendrites growth on PCF.

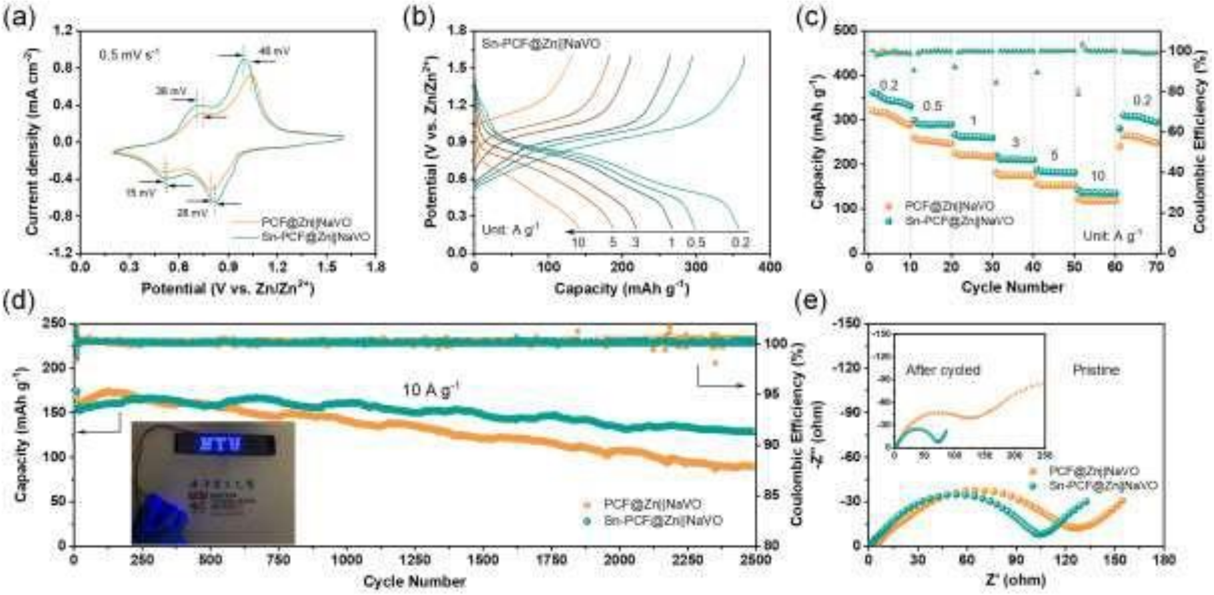

Fig. 5 Full cells with NaVO cathode. (a) CV profiles, (b) charge-discharge curves, and (c) rate performance. (d) Long-term cycling performance at 10 A g^{-1}. Inset is a 3.7 V LED array powered by four-coin cells. (e) Nyquist plots of the cells before and after cycling test at 10 A g^{-1}.

The cycle stabilities were investigated through galvanostatic charge/discharge test. A discharge capacity of 242 mAh g^{-1} can be maintained in Sn-PCF@Zn||NaVO after 300 cycles at 1 A g^{-1} (Fig. S19), much superior to that of the cell with PCF@Zn (180 mAh g^{-1}) and Cu@Zn (155 mAh g^{-1} after 100 cycles). The polygonal Zn flakes combined with porous surface on Cu@Zn and PCF@Zn anodes can be well distinguished from the *ex-situ* SEM images (Fig. S20). In contrast, Sn-PCF@Zn remains a dense dendrites morphology, suggesting that the regulation of Zn deposition on Sn-PCF is still stable and effective in full cells. In the long-term cycling test at 5 A g^{-1} (Fig. S21), a discharge capacity of 150 mAh g^{-1} can be retained in Sn-PCF@Zn based battery after 2000 cycles with a decay rate of 0.009 % per cycle. Even the current density goes up to 10 A g^{-1} (Fig. 5d), a high initial discharge capacity of 174 mAh^{-1} can be realized, and an impressive capacity retention around 73.5 %

can still be maintained after 2500 cycles (i.e., capacity attenuation rate of 0.010 % per cycle). According to the XRD patterns after cycling (Fig. S22), there are much less ZSH passivation on Sn-PCF than that on PCF because of the HER prohibition. ZSH is considered as an ion/electron insulator which will significantly enhance the polarization during the charge-discharge process. Referring to the equivalent circuit and Nyquist plots (Fig. 5e and S23), Sn-PCF@Zn||NaVO battery reveals a lower charge transfer resistance than that of PCF@Zn||NaVO (Table S1). Hence, the above results strongly attest that the Sn-PCF as with homogenized Zn nucleation, limited side-reactions and high structural robustness has significantly boosted the durability of AZBs.

Apart from Zn deposition, such a 3D conductive scaffold could also be applied for deposition of other metals such as Li, Na, K, and Al. In addition, owing to the crosslinked conductive framework, the insulating active species with large volume fluctuation during charge/discharge cycles could also be well accommodated by our 3D PCF, such as S, Se, and I.

3. Conclusions

A new Sn-deposited porous carbon fibers (Sn-PCF) 3D micro-scaffold has been fabricated and employed as the host for Zn metal anode that successfully suppress the detrimental hydrogen evolution and dendrites formation, leading to improved cycle performance in aqueous Zn battery. A 3D porous carbon fibers micro-scaffold effectively lowers the local current density, uniformizes the electric field, and can also physically confine the dendrites. Experiments and calculation reveal that metallic Sn with strong Zn^{2+} adsorption and high Zn^{2+} surface diffusion barrier is the key to the regulated nucleation and homogeneous Zn deposition on each individual carbon fiber. Meanwhile, passivation due to ZSH byproduct has also been eliminated owing to a lowered hydrogen evolution reaction tendency on the Sn surface. These factors have rendered the Sn-PCF@Zn electrode with low polarization, fast redox kinetics and stable coulombic efficiency at various current densities (1-20 mA cm^{-2}). As a result, a high reversibility of Zn plating/stripping and outstanding cycling stability in $Na_2V_6O_{16}$ || Sn-PCF@Zn full devices have been achieved. The presented strategy may provide an ideal solution to address the critical issues of Zn anode and to advance the progress of long-lifespan aqueous Zn batteries.

Declaration of Competing Interest

The authors declare no competing interests.

Supporting Information

Supplementary material associated with this article can be found, in the online version, at doi: xxx.

Credit author statement

Jin-Lin Yang: Conceptualization, Methodology, Investigation, Writing – original draft, Visualization. **Peihua Yang:** Writing – Reviewing and Editing. **Wenqi Yan:** Methodology. **Jian-Wei Zhao:** Methodology, Software. **Hong Jin Fan:** Supervision, Project administration, Funding acquisition, Conceptualization.

Acknowledgement

This work was supported from...

REFERENCES

[1] D. Chao, C.R. Zhu, M. Song, P. Liang, X. Zhang, N.H. Tiep, H. Zhao, J. Wang, R. Wang, H. Zhang, H.J. Fan, A high-rate and stable quasi-solid-state zinc-ion battery with novel 2D layered zinc orthovanadate array, Adv. Mater. 30 (2018) 1803181, doi: 10.1002/adma.201803181.

[2] J. Xie, Q. Zhang, Recent progress in aqueous monovalent-ion batteries with organic materials as promising electrodes, Mater. Today Energy 18 (2020) 100547, doi: 10.1016/j.mtener.2020.100547.

[3] S. Bi, Y. Wu, A. Cao, J. Tian, S. Zhang, Z. Niu, Free-standing three-dimensional carbon nanotubes/amorphous MnO_2 cathodes for aqueous zinc-ion batteries with superior rate performance, Mater. Today Energy 18 (2020) 100548, doi: 10.1016/j.mtener.2020.100548.

[4] P. Yang, J. Li, S.W. Lee, H.J. Fan, Printed zinc paper batteries, Adv. Sci. 9 (2022) 2103894, doi: 10.1002/advs.202103894.

[5] H. Jia, Z. Wang, B. Tawiah, Y. Wang, C.-Y. Chan, B. Fei, F. Pan, Recent advances in zinc

anodes for high-performance aqueous Zn-ion batteries, Nano Energy 70 (2020) 104523, doi: 10.1016/j.nanoen.2020.104523.

[6] J.H. Park, M.J. Kwak, C. Hwang, K.N. Kang, N. Liu, J.H. Jang, B.A. Grzybowski, Self-assembling films of covalent organic frameworks enable long-term, efficient cycling of zinc-ion batteries, Adv. Mater. 33 (2021) 2101726, doi: 10.1002/adma.202101726.

[7] Y. Tian, Y. An, C. Wei, B. Xi, S. Xiong, J. Feng, Y. Qian, Recent advances and perspectives of Zn-metal free “rocking-chair”-type Zn-ion batteries, Adv. Energy Mater. 11 (2020) 2002529, doi: 10.1002/aenm.202002529.

[8] Y. Zuo, K. Wang, P. Pei, M. Wei, X. Liu, Y. Xiao, P. Zhang, Zinc dendrite growth and inhibition strategies, Mater. Today Energy 20 (2021) 100692, doi: 10.1016/j.mtener.2021.100692.

[9] T.H. Wu, Y. Zhang, Z.D. Althouse, N. Liu, Nanoscale design of zinc anodes for high-energy aqueous rechargeable batteries, Mater. Today Nano 6 (2019) 100032, doi: 10.1016/j.mtnano.2019.100032.

[10] S. Higashi, S.W. Lee, J.S. Lee, K. Takechi, Y. Cui, Avoiding short circuits from zinc metal dendrites in anode by backside-plating configuration, Nat. Commun. 7 (2016) 11801, doi: 10.1038/ncomms11801.

[11] Y. Zhang, Z. Cao, S. Liu, Z. Du, Y. Cui, J. Gu, Y. Shi, B. Li, S. Yang, Charge-enriched strategy based on mxene-based polypyrrole layers toward dendrite-free zinc metal anodes, Adv. Energy Mater. 12 (2022) 2103979, doi: 10.1002/aenm.202103979.

[12] M. Cui, Y. Xiao, L. Kang, W. Du, Y. Gao, X. Sun, Y. Zhou, X. Li, H. Li, F. Jiang, C. Zhi, Quasi-isolated Au particles as heterogeneous seeds to guide uniform Zn deposition for aqueous zinc-ion batteries, ACS Appl. Energy Mater. 2 (2019) 6490-6496, doi: 10.1021/acsaem.9b01063.

[13] M. Zhou, Y. Chen, G. Fang, S. Liang, Electrolyte/electrode interfacial electrochemical behaviors and optimization strategies in aqueous zinc-ion batteries, Energy Storage Mater. 45 (2022) 618-646, doi: 10.1016/j.ensm.2021.12.011.

[14] J. Zheng, Q. Zhao, T. Tang, J. Yin, C.D. Quilty, G.D. Renderos, X. Liu, Y. Deng, L. Wang, D.C. Bock, Reversible epitaxial electrodeposition of metals in battery anodes, Science 366 (2019) 645-648, doi: 10.1126/science.aax6873.

[15] Q. Yang, Y. Guo, B. Yan, C. Wang, Z. Liu, Z. Huang, Y. Wang, Y. Li, H. Li, L. Song, J. Fan, C. Zhi, Hydrogen-substituted graphdiyne ion tunnels directing concentration redistribution for commercial-grade dendrite-free zinc anodes, Adv. Mater. 32 (2020) 2001755, doi: 10.1002/adma.202001755.

[16] S. Guo, L. Qin, T. Zhang, M. Zhou, J. Zhou, G. Fang, S. Liang, Fundamentals and perspectives of electrolyte additives for aqueous zinc-ion batteries, Energy Storage Mater. 34 (2021) 545-562, doi: 10.1016/j.ensm.2020.10.019.

[17] K. Wu, J. Yi, X. Liu, Y. Sun, J. Cui, Y. Xie, Y. Liu, Y. Xia, J. Zhang, Regulating Zn deposition via an artificial solid-electrolyte interface with aligned dipoles for long life Zn anode, Nano-Micro Lett. 13 (2021) 79, doi: 10.1007/s40820-021-00599-2.

[18] J.-L. Yang, J. Li, J.-W. Zhao, K. Liu, P. Yang, H.J. Fan, Stable zinc anodes enabled by a zincophilic polyanionic hydrogel layer, Adv. Mater. 34 (2022) 2202382, doi: 10.1002/adma.202202382.

[19] W. Guo, Z. Cong, Z. Guo, C. Chang, X. Liang, Y. Liu, W. Hu, X. Pu, Dendrite-free Zn anode with dual channel 3D porous frameworks for rechargeable Zn batteries, Energy Storage Mater. 30 (2020) 104-112, doi: 10.1016/j.ensm.2020.04.038.

[20] Z. Kang, C. Wu, L. Dong, W. Liu, J. Mou, J. Zhang, Z. Chang, B. Jiang, G. Wang, F. Kang, C. Xu, 3D porous copper skeleton supported zinc anode toward high capacity and long cycle life zinc ion batteries, ACS Sustainable Chem. Eng. 7 (2019) 3364-3371, doi: 10.1021/acssuschemeng.8b05568.

[21] G. Zhang, X. Zhang, H. Liu, J. Li, Y. Chen, H. Duan, 3D-printed multi-channel metal

lattices enabling localized electric-field redistribution for dendrite-free aqueous Zn ion batteries, Adv. Energy Mater. 11 (2021) 2003927, doi: 10.1002/aenm.202003927.

[22] Y. Yin, S. Wang, Q. Zhang, Y. Song, N. Chang, Y. Pan, H. Zhang, X. Li, Dendrite-free zinc deposition induced by tin-modified multifunctional 3D host for stable zinc-based flow battery, Adv. Mater. 32 (2020) 1906803, doi: 10.1002/adma.201906803.

[23] Z. Wang, J. Huang, Z. Guo, X. Dong, Y. Liu, Y. Wang, Y. Xia, A metal-organic framework host for highly reversible dendrite-free zinc metal anodes, Joule 3 (2019) 1289-1300, doi: 10.1016/j.joule.2019.02.012.

[24] Y. Zeng, X. Zhang, R. Qin, X. Liu, P. Fang, D. Zheng, Y. Tong, X. Lu, Dendrite-free zinc deposition induced by multifunctional CNT frameworks for stable flexible Zn-ion batteries, Adv. Mater. 31 (2019) 1903675, doi: 10.1002/adma.201903675.

[25] Y. Zhou, X. Wang, X. Shen, Y. Shi, C. Zhu, S. Zeng, H. Xu, P. Cao, Y. Wang, J. Di, Q. Li, 3D confined zinc plating/stripping with high discharge depth and excellent high-rate reversibility, J. Mater. Chem. A 8 (2020) 11719-11727, doi: 10.1039/d0ta02791j.

[26] Z. Li, B.Y. Guan, J. Zhang, X.W. Lou, A compact nanoconfined sulfur cathode for high-performance lithium-sulfur batteries, Joule 1 (2017) 576-587, doi: 10.1016/j.joule.2017.06.003.

[27] Y. Fang, S.L. Zhang, Z.-P. Wu, D. Luan, X.W. Lou, A highly stable lithium metal anode enabled by Ag nanoparticle-embedded nitrogen-doped carbon macroporous fibers, Sci. Adv. 7 (2021) eabg3626, doi: 10.1126/sciadv.abg3626.

[28] J.L. Yang, S.X. Zhao, X.T. Zeng, Y.M. Lu, G.z. Cao, Catalytic interfaces-enriched hybrid hollow spheres sulfur host for advanced Li–S batteries, Adv. Mater. Interfaces 7 (2019) 1901420, doi: 10.1002/admi.201901420.

[29] J.L. Yang, D.Q. Cai, X.G. Hao, L. Huang, Q. Lin, X.T. Zeng, S.X. Zhao, W. Lv, Rich heterointerfaces enabling rapid polysulfides conversion and regulated Li_2S deposition for high-performance lithium-sulfur batteries, ACS Nano 15 (2021) 11491-11500, doi: 10.1021/acsnano.1c01250.

[30] L. Wang, W. Huang, W. Guo, Z.H. Guo, C. Chang, L. Gao, X. Pu, Sn alloying to inhibit hydrogen evolution of Zn metal anode in rechargeable aqueous batteries, Adv. Funct. Mater. 32 (2021) 2108533, doi: 10.1002/adfm.202108533.

[31] H. Yu, Y. Zeng, W. Li Nian, D. Luan, L. Yu, W. Lou Xiong, Confining Sn nanoparticles in interconnected N-doped hollow carbon spheres as hierarchical zincophilic fibers for dendrite-free Zn metal anodes, Sci. Adv. 8 (2022) eabm5766, doi: 10.1126/sciadv.abm5766.

[32] Z. Hou, Y. Gao, H. Tan, B. Zhang, Realizing high-power and high-capacity zinc/sodium metal anodes through interfacial chemistry regulation, Nat. Commun. 12 (2021) 3083, doi: 10.1038/s41467-021-23352-0.

[33] Y. Guo, X. Zeng, Y. Zhang, Z. Dai, H. Fan, Y. Huang, W. Zhang, H. Zhang, J. Lu, F. Huo, Q. Yan, Sn nanoparticles encapsulated in 3D nanoporous carbon derived from a metal-organic framework for anode material in lithium-ion batteries, ACS Appl. Mater. Interfaces 9 (2017) 17172-17177, doi: 10.1021/acsami.7b04561.

[34] P. Xue, C. Guo, N. Wang, K. Zhu, S. Jing, S. Kong, X. Zhang, L. Li, H. Li, Y. Feng, W. Gong, Q. Li, Synergistic manipulation of Zn^{2+} ion flux and nucleation induction effect enabled by 3D hollow SiO_2/TiO_2/carbon fiber for long-lifespan and dendrite-free Zn–metal composite anodes, Adv. Funct. Mater. 31 (2021) 2106417, doi: 10.1002/adfm.202106417.

[35] Z. Xu, S. Jin, N. Zhang, W. Deng, M.H. Seo, X. Wang, Efficient Zn metal anode enabled by O,N-codoped carbon microflowers, Nano Lett. 22 (2022) 1350-1357, doi: 10.1021/acs.nanolett.1c04709.

[36] J. Guo, W. Zhang, J. Yin, Y. Zhu, Z.O.F. Mohammed, H.N. Alshareef, Zincophilic laser-scribed graphene interlayer for homogeneous zinc deposition and stable zinc-ion batteries, Energy Technol. 9 (2021) 2100490, doi: 10.1002/ente.202100490.

[37] Q. Jian, Z. Guo, L. Zhang, M. Wu, T. Zhao, A hierarchical porous tin host for

dendrite-free, highly reversible zinc anodes, Chem. Eng. J. 425 (2021) 130643, doi: 10.1016/j.cej.2021.130643.

[38] D. Lee, H.I. Kim, W.Y. Kim, S.K. Cho, K. Baek, K. Jeong, D.B. Ahn, S. Park, S.J. Kang, S.Y. Lee, Water-repellent ionic liquid skinny gels customized for aqueous Zn-ion battery anodes, Adv. Funct. Mater. 31 (2021) 2103850, doi: 10.1002/adfm.202103850.

[39] Y. Tian, Y. An, C. Wei, B. Xi, S. Xiong, J. Feng, Y. Qian, Flexible and free-standing $Ti_3C_2T_x$ MXene@Zn paper for dendrite-free aqueous zinc metal batteries and nonaqueous lithium metal batteries, ACS Nano 13 (2019) 11676-11685, doi: 10.1021/acsnano.9b05599.

[40] C. Li, X. Shi, S. Liang, X. Ma, M. Han, X. Wu, J. Zhou, Spatially homogeneous copper foam as surface dendrite-free host for zinc metal anode, Chem. Eng. J. 379 (2020) 122248, doi: 10.1016/j.cej.2019.122248.

[41] Q. Zhang, J. Luan, X. Huang, L. Zhu, Y. Tang, X. Ji, H. Wang, Simultaneously regulating the ion distribution and electric field to achieve dendrite-free Zn anode, Small 16 (2020) 2000929, doi: 10.1002/smll.202000929.

[42] Y. An, Y. Tian, S. Xiong, J. Feng, Y. Qian, Scalable and controllable synthesis of interface-engineered nanoporous host for dendrite-free and high rate zinc metal batteries, ACS Nano 15 (2021) 11828-11842, doi: 10.1021/acsnano.1c02928.

[43] F. Wan, L. Zhang, X. Dai, X. Wang, Z. Niu, J. Chen, Aqueous rechargeable zinc/sodium vanadate batteries with enhanced performance from simultaneous insertion of dual carriers, Nat. Commun. 9 (2018) 1656, doi: 10.1038/s41467-018-04060-8.

[44] P. Hu, T. Zhu, X. Wang, X. Wei, M. Yan, J. Li, W. Luo, W. Yang, W. Zhang, L. Zhou, Z. Zhou, L. Mai, Highly durable $Na_2V_6O_{16}\cdot1.63H_2O$ nanowire cathode for aqueous zinc-ion battery, Nano Lett. 18 (2018) 1758-1763, doi: 10.1021/acs.nanolett.7b04889.

[45] Y. Yang, C. Liu, Z. Lv, H. Yang, Y. Zhang, M. Ye, L. Chen, J. Zhao, C.C. Li, Synergistic manipulation of Zn^{2+} ion flux and desolvation effect enabled by anodic growth of a 3D ZnF_2 matrix for long-lifespan and dendrite-free Zn metal anodes, Adv. Mater. 33 (2021) 2007388, doi: 10.1002/adma.202007388.